

Experimental characterization of a spin quantum heat engine

John P. S. Peterson,^{1,*} Tiago B. Batalhão,^{2,3,4,*} Marcela Herrera,^{2,*} Alexandre M. Souza,⁵ Roberto S. Sarthour,⁵ Ivan S. Oliveira,⁵ and Roberto M. Serra^{2,†}

¹*Institute for Quantum Computing and Department of Physics and Astronomy, University of Waterloo, Waterloo N2L 3G1, Ontario, Canada*

²*Centro de Ciências Naturais e Humanas, Universidade Federal do ABC, Avenida dos Estados 5001, 09210-580 Santo André, São Paulo, Brazil*

³*Singapore University of Technology and Design, 8 Somapah Road, Singapore 487372, Singapore*

⁴*Centre for Quantum Technologies, National University of Singapore, 3 Science Drive 2, Singapore 117543, Singapore*

⁵*Centro Brasileiro de Pesquisas Físicas, Rua Dr. Xavier Sigaud 150, 22290-180 Rio de Janeiro, Rio de Janeiro, Brazil*

Developments in the thermodynamics of small quantum systems envisage non-classical thermal machines. In this scenario, energy fluctuations play a relevant role in the description of irreversibility. We experimentally implement a quantum heat engine based on a spin-1/2 system and nuclear magnetic resonance techniques. Irreversibility at microscope scale is fully characterized by the assessment of energy fluctuations associated with the work and heat flows. We also investigate the efficiency lag related to the entropy production at finite time. The implemented heat engine operates in a regime where both thermal and quantum fluctuations (associated with transitions among the instantaneous energy eigenstates) are relevant to its description. Performing a quantum Otto cycle at maximum power, the proof-of-concept quantum heat engine is able to reach an efficiency for work extraction ($\eta \approx 42\%$) very close to its thermodynamic limit ($\eta = 44\%$).

Quantum thermal machines perform a thermodynamic cycle employing quantum systems as the working medium. This notion was introduced long ago when Scovil and Schulz-Dubois recognized a three-level maser as a kind of heat engine [1], and since then many theoretical proposals for thermodynamical cycles at the quantum scale have been discussed [2–32]. Microscopic quantum heat engines may operate at a scale where both thermal and quantum fluctuations are relevant. The thermodynamic description of such devices operating at finite time should also include the inherent non-deterministic nature of the quantum evolution and non-equilibrium features. In this context, quantities as work, heat, and entropy production are associated with statistical distributions that satisfy fluctuation theorems [33–35] for a thermodynamical cycle [36, 37].

The enthusiastic interest in quantum thermal machines has grown with the possibility to control non-equilibrium dynamics of microscopic systems, achievable in platforms such as: trapped ions [38, 39], quantum dots [40–42], single electron boxes [43], optomechanical oscillators [44–47], etc. Some experimental success related to the implementation of micro-scale heat engines have been reported in a context where quantum coherence effects are not prominent (which can be regarded as a classical context) [48–53]. Recently, a single trapped ion was employed as a working medium to perform a thermodynamic cycle [54]. Despite this latter implementation being based on a single quantum system, the operating temperatures are such that the thermal energy is considerably higher than the energy level separation of the magnetic trap. As a consequence, effects of quantum fluctuations are dwarfed by thermal fluctuations allowing a classical description.

The full characterization of a finite-time operation of a quantum heat engine may also be associated with the assessment of the probability distribution of energy fluctuations, that can take the form of work or heat flow [55]. This assessment embodies significant experimental challenges that remained elusive up to now.

In the present contribution, we used a Nuclear Magnetic Resonance (NMR) setup [56] to implement and characterize a quantum version of the Otto cycle [4]. As a proof-of-concept implementation of a quantum heat engine operating at finite time, we employed a ^{13}C -labeled CHCl_3 liquid sample diluted in Acetone- D_6 and a 500 MHz Varian NMR spectrometer. The spin 1/2 of the ^{13}C nucleus is the working medium whereas the ^1H nuclear spin will be used as a heat bus. High radio-frequency (rf) modes near to Hydrogen Larmor frequency plays the role of the hot environment while low rf modes near to Carbon resonance frequency plays the role of the cold environment. Chlorine isotopes' nuclei provide mild environmental effects. An interferometric method [57–61] is applied to assess energy fluctuations to characterize the work and heat statistics as well as the irreversibility aspects of this spin engine. The operation regime is such that the typical thermal energy scale is of the same order of the typical separation of the quantum energy levels, turning the effects of quantum fluctuations as important as the ones from thermal fluctuations. We have also experimentally endorsed an expression for the efficiency lag related to the entropy production that hinders the implemented engine to attain the Carnot efficiency at finite time. The cycle was established at different finite-time regimes, ranging from a very irreversible to one with almost maximum efficiency, allowing the identification of

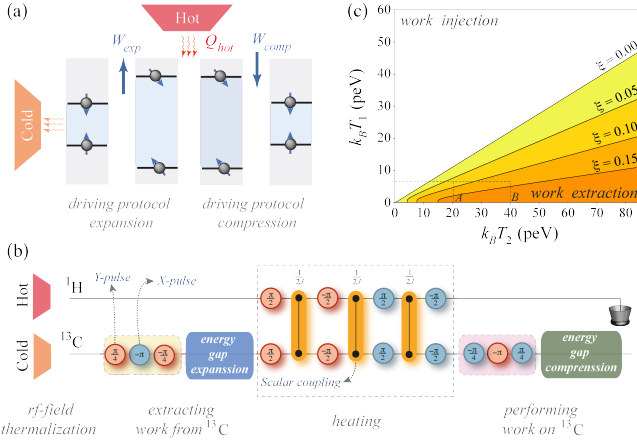


Figure 1. Quantum heat engine schematics. (a) Thermodynamic cycle employing a spin 1/2 as working medium. (b) Simplified pulse sequence of the experimental protocol. ^1H and ^{13}C nuclear spins are initially prepared in thermal states corresponding to hot and cold spin temperatures, respectively. Blue (red) circles represent x (y) rotations by the displayed angle produced by transverse rf pulses. Orange connections stand for free evolutions under the scalar interaction (\mathcal{H}_J) during the time displayed above the symbol. The unitary driving for the energy gap expansion (compression) protocol is implemented by a time-modulated rf field resonant with the ^{13}C nuclear spin. The Hydrogen nucleus is used to deliver the heat at the proper part of the cycle, working as a heat bus. (c) Required temperatures for work extraction at finite-time operation mode. The engine extracts work only if the hot (T_2) and cold (T_1) source temperatures correspond to a point below the curve defined by the energy level transition probability ξ .

the maximum power operation.

The quantum version of the Otto cycle [4, 20] consists of a four-stroke protocol as illustrated in Fig. 1(a).

Cooling stroke. Using spatial average techniques employed by rf and gradient fields, the ^{13}C nuclear spin is initially chilled to a pseudo-thermal state, equivalent to $\rho_0^{eq,1} = e^{-\beta_1 \mathcal{H}_1^C} / Z_1$ [62, 63], at a cold inverse spin temperature $\beta_1 = (k_B T_1)^{-1}$, where $Z_1 = \text{tr}(e^{-\beta_1 \mathcal{H}_1^C})$ is the partition function, k_B is the Boltzmann constant, T_1 is the absolute spin temperature of the cold reference state, and the Hamiltonian \mathcal{H}_1^C will be defined latter.

Expansion stroke. The working medium Hamiltonian is driven by a time-modulated rf field resonant with the ^{13}C nuclear spin. Initially it can be described by $\mathcal{H}_1^C = -h\nu_1 \sigma_y^C / 2$ (with the rf-field intensity adjusted such that $\nu_1 = 2.0$ kHz and $\sigma_{x,y,z}^C$ being the Pauli spin operators for ^{13}C nuclear spin), in a rotating frame at the ^{13}C Larmor frequency (≈ 125 MHz). From $t = 0$ up to $t = \tau$, the system Hamiltonian is driving according to $\mathcal{H}_{exp}^C(t) = -\frac{1}{2}h\nu(t) (\cos(\frac{\pi t}{2\tau}) \sigma_x^C + \sin(\frac{\pi t}{2\tau}) \sigma_y^C)$, expanding (*exp*) the nuclear spin energy gap linearly as $\nu(t) = \nu_1 (1 - \frac{t}{\tau}) + \nu_2 \frac{t}{\tau}$ (with $\nu_2 = 3.6$ kHz and $t \in [0, \tau]$).

The energy gap expansion happens in a driving time length, τ , that will be varied in different experiments between $100 \mu\text{s}$ and $700 \mu\text{s}$. The driving time length ($\propto 10^{-4}\text{s}$) is much shorter than the typical decoherence time scales, which are on the order of seconds. In this way, we can describe this process by a unitary evolution, \mathcal{U}_τ [59, 61, 63], that drives the ^{13}C nuclear spin to an out-of-equilibrium state (ρ_τ^C), which is, in general, not diagonal in the energy eigenbasis of the final Hamiltonian of the expansion protocol, $\mathcal{H}_2^C = \mathcal{H}_{exp}^C(\tau) = -h\nu_2 \sigma_x^C / 2$.

Heating stroke. The working medium (^{13}C nucleus) exchanges heat with the ^1H nuclear spin, which was initially prepared in a higher temperature [62, 63] than the ^{13}C nuclear spin, reaching full thermalization at the hot inverse spin temperature $\beta_2 = (k_B T_2)^{-1}$. The full thermalization process is effectively implemented by a sequence of free evolutions under the scalar interaction, $\mathcal{H}_J = \frac{1}{2}hJ\sigma_z^H\sigma_z^C$ (with $J \approx 215.1$ Hz), between both nuclei and rf pulses to produce suitable rotations as sketched in Fig. 1(b). After thermalization, the state of the ^{13}C nuclei is the hot equilibrium state, equivalent to $\rho_0^{eq,2} = e^{-\beta_2 \mathcal{H}_2^C} / Z_2$.

Compression stroke. Subsequently, an energy gap compression is performed, according to the time-reversed process [64] of the expansion protocol, i.e., the Hamiltonian is driven in a way that $\mathcal{H}_{comp}^C(t) = -\mathcal{H}_{exp}^C(\tau - t)$.

Many cycles of this proof-of-concept experiment can be performed repeating successively the pulse sequence protocol described in Fig. 1(b). It is interesting to note that each experimental run involves spatial averages on a diluted liquid sample containing about 10^{17} molecules, which can be regarded as noninteracting with each other due to the sample dilution. Each experimental result for the quantities of interest represents an average over many copies of a single molecular spin engine.

The finite-time (expansion and compression) driven processes are associated with transitions among the instantaneous eigenstates of the working medium Hamiltonian (see Fig. S3 of [63]) resulting in entropy production [61, 65], which is the main source of irreversibility in the implemented cycle. In this way, quantum coherence also contributes to the irreversibility [66–68].

Considering the aforementioned description of the finite-time thermodynamical cycle, we can write the average values of the extracted work (W_{eng}) from the engine and the absorbed heat (Q_{hot}) from the ^1H nuclear spin as

$$\langle W_{eng} \rangle = \frac{h}{2} (\nu_2 - \nu_1) [\tanh(\beta_1 h\nu_1) - \tanh(\beta_2 h\nu_2)] - h\xi [\nu_1 \tanh(\beta_2 h\nu_2) + \nu_2 \tanh(\beta_1 h\nu_1)], \quad (1)$$

$$\langle Q_{hot} \rangle = \frac{h}{2} \nu_2 [\tanh(\beta_1 h\nu_1) - \tanh(\beta_2 h\nu_2)] - \xi h\nu_2 \tanh(\beta_1 h\nu_1), \quad (2)$$

where $\xi = |\langle \Psi_{\pm}^2 | \mathcal{U}_{\tau} | \Psi_{\mp}^1 \rangle|^2 = |\langle \Psi_{\pm}^1 | \mathcal{V}_{\tau} | \Psi_{\mp}^2 \rangle|^2$ are the transition probabilities between the instantaneous eigenstates $|\Psi_{\pm}^1\rangle$ ($|\Psi_{\pm}^2\rangle$) of the Hamiltonian \mathcal{H}_1^C (\mathcal{H}_2^C) and \mathcal{V}_{τ} is the unitary evolution describing the compression protocol, satisfying $\mathcal{V}_{\tau} = \mathcal{U}_{\tau}^{\dagger}$. The nuclear spin system operates as a heat engine when $\langle W_{eng} \rangle > 0$, otherwise work is being injected in the device during the cycle. Two conditions must be met to allow work extraction. The first is the requirement that $(\nu_2 - \nu_1) [\tanh(\beta_1 h \nu_1) - \tanh(\beta_2 h \nu_2)] \geq 0$, which is equivalent to the classical-scenario bound, $1 \leq \nu_2/\nu_1 \leq T_2/T_1$. The second condition imposes a limit on the admitted transition probability among the energy levels, which reads

$$\xi \leq \frac{(\nu_2 - \nu_1) [\tanh(\beta_1 h \nu_1) - \tanh(\beta_2 h \nu_2)]}{2 [\nu_1 \tanh(\beta_2 h \nu_2) + \nu_2 \tanh(\beta_1 h \nu_1)]}. \quad (3)$$

This condition, illustrated in Fig. 1(c), is related to the rapidity of the energy gap expansion (compression) protocol and to the fact that the driving Hamiltonian does not commute at different times. For a given protocol (that sets the ξ value) the condition (3) only depends on the energy gap compression factor, $r = \nu_2/\nu_1$ ($r \simeq 1.8$ in our experiment). The system operates in the working extraction mode if the point that characterizes the temperature of both heat sources lies below the contour curve in Fig. 1(c) for a given transition probability.

The spin-engine efficiency can be written also in terms of the energy level transition probability as

$$\eta = \frac{\langle W_{eng} \rangle}{\langle Q_{hot} \rangle} = 1 - \frac{\nu_1 (1 - 2\xi\mathcal{F})}{\nu_2 (1 - 2\xi\mathcal{G})}, \quad (4)$$

where $\mathcal{F} = \tanh(\beta_2 h \nu_2) (\tanh(\beta_2 h \nu_2) - \tanh(\beta_1 h \nu_1))^{-1}$ and $\mathcal{G} = \mathcal{F} \tanh(\beta_1 h \nu_1) / \tanh(\beta_2 h \nu_2)$. The Otto limit (η_{Otto}) is recovered in an adiabatic (transitionless, i.e. $\xi = 0$) driving. On the other hand, in the finite-time regime the efficiency (4) decreases as ξ increases. Alternatively, we can derive an expression for the engine efficiency in terms of efficiency lags (associated with entropy production [29–31, 61]) as $\eta = \eta_{\text{Carnot}} - \mathcal{L}$, and the lag is given by [63]

$$\mathcal{L} = \frac{\mathcal{S}(\mathcal{U}_{\tau} \rho_0^{eq,1} \mathcal{U}_{\tau}^{\dagger} \parallel \rho_0^{eq,2}) + \mathcal{S}(\mathcal{V}_{\tau} \rho_0^{eq,2} \mathcal{V}_{\tau}^{\dagger} \parallel \rho_0^{eq,1})}{\beta_1 \langle Q_{hot} \rangle}, \quad (5)$$

where $\mathcal{S}(\rho_a \parallel \rho_b) = \text{tr}[\rho_a (\ln \rho_a - \ln \rho_b)]$ is the relative entropy and $\eta_{\text{Carnot}} = 1 - T_1/T_2$ the standard Carnot efficiency.

Work extracted from (performed on) the ^{13}C nuclear spin during the energy gap expansion (compression) driving protocol is actually a stochastic variable, described by a probability distribution [36, 37], $P_{exp}(W)$ ($P_{comp}(W)$). The full thermalization with the hot source allows us to write the work performed in each Hamiltonian driving stroke of the cycle as independent variables. So, the net

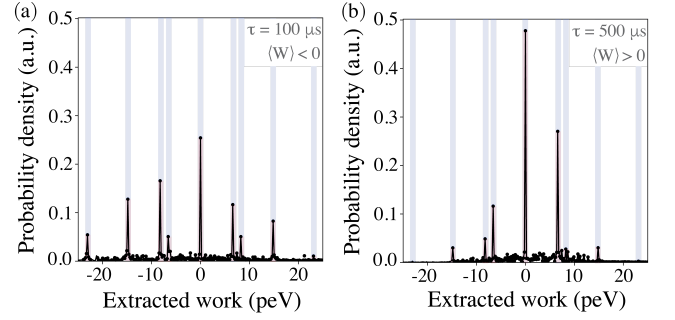


Figure 2. Extracted work probability distribution of the quantum engine with Hamiltonian driving time lengths: (a) $\tau = 100 \mu\text{s}$ and (b) $\tau = 500 \mu\text{s}$. Cold and hot source temperatures are set at $k_B T_1 = (6.6 \pm 0.1) \text{ peV}$ and $k_B T_2^B = (40.5 \pm 3.7) \text{ peV}$, respectively. The experimental data (points) is well fitted by a sum of nine Lorentzian peaks (the full line) centered approximately at $0, \pm h(\nu_2 - \nu_1), \pm \nu_1, \pm \nu_2$, and $\pm h(\nu_2 + \nu_1)$ (dashed columns), in agreement with the theoretical expectation (see supplemental Fig. S3 in [63]). The error bars are smaller than the symbols size and are not shown.

extracted work from the engine is a convolution of the two marginal work probability distributions, which can be assessed by the interferometric approach [59, 61]. In the present experiment, the characteristic function of the work probability distribution is measured. In the energy gap expansion stroke, it is given by

$$\begin{aligned} \chi_{exp}(u) &= \text{tr} \left[\mathcal{U}_{\tau} e^{-iu\mathcal{H}_{exp,0}^C} \rho_0^{eq,1} \left(e^{-iu\mathcal{H}_{exp,\tau}^C} \mathcal{U}_{\tau} \right)^{\dagger} \right] \\ &= \sum_{n,m=0}^1 p_n^0 p_{m|n}^{\tau} e^{iu(\epsilon_m^{\tau} - \epsilon_n^0)}, \end{aligned} \quad (6)$$

where p_n^0 is the occupation probability of the n -th energy level in the cold initial thermal state ($\rho_0^{eq,1}$), $p_{m|n}^{\tau} = \xi + (1 - 2\xi) \delta_{m,n}$ is the transition probability between the Hamiltonian eigenstates induced by the time-dependent quantum dynamics, ϵ_m^{τ} and ϵ_n^0 are eigenenergies of the Hamiltonians \mathcal{H}_1^C and \mathcal{H}_2^C , respectively. Analogous expressions hold for the compression stroke ($\chi_{comp}(u)$) [63]. The characteristic function for the engine net work is the product of characteristic functions for both Hamiltonian driving protocols, i.e. $\chi_{eng}(u) = \chi_{comp}(u)\chi_{exp}(u)$. Thus, the inverse Fourier transform of the measured $\chi_{eng}(u)$ provides the work probability distribution for the quantum engine as $P_{eng}(W) = \int du \chi_{eng}(u) e^{iuW}$ and the mean value of the extracted work can be obtained from the statistics as $\langle W_{eng} \rangle = \int dW P_{eng}(W) W$.

We characterized the work distribution in different operation modes of the spin engine, varying the driving time length (τ) and the hot source temperature, with representative results displayed in Fig. 2. The initial spin temperatures of the ^1H and ^{13}C nuclei were verified by quantum

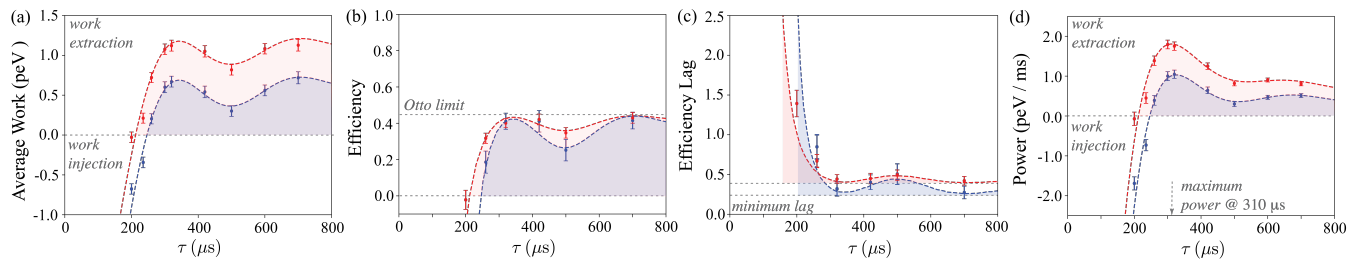


Figure 3. Spin quantum engine figures of merit: (a) average extracted work, (b) efficiency, (c) efficiency lag due to entropy production cf. Eq. (5) (the minimum lag is $\eta_{\text{Carnot}} - \eta_{\text{Otto}}$), and (d) extracted power, as a function of the driving protocol time length (τ). Points represent experimental data. The dashed lines are based on theoretical predictions and numerical simulations. In all experiments, the spin temperature of the cold source is set at $k_B T_1 = (6.6 \pm 0.1)$ peV. Data in blue and red correspond to implementations with the hot source spin temperatures set at $k_B T_2^A = (21.5 \pm 0.4)$ peV and $k_B T_2^B = (40.5 \pm 3.7)$ peV, respectively.

state tomography (QST) [56], which confirmed the Gibbs state preparation. The spin temperature of the ^{13}C cold initial state is equivalent to $k_B T_1 = (6.6 \pm 0.1)$ peV, while the ^1H was prepared in two hot states (A and B) corresponding to $k_B T_2^A = (21.5 \pm 0.4)$ peV and $k_B T_2^B = (40.5 \pm 3.7)$ peV.

There are nine observed peaks in Fig. 2(a), corresponding to the fastest implemented engine driving. A fit of these experimental data allows us to determine the transition probability ξ that vary from $\xi = 0.02 \pm 0.02$ (for $\tau = 700 \mu\text{s}$) to $\xi = 0.38 \pm 0.04$ (for $\tau = 100 \mu\text{s}$). We observe that when the Hamiltonian driving is slower, as in Fig. 2(b), some of the work distribution peaks get decreased to the point of being barely noticeable amid the noise (associated with the Fourier analysis), since the dynamics is getting closer to the adiabatic one. We also characterize the Hamiltonian driving protocol by means of quantum process tomography [69, 70] to certify that it implements an almost unitary process [63].

The absorbed heat from the hot source (^1H nuclear spin) is also a stochastic variable and its probability distribution, $\mathcal{P}(Q)$, could be assessed by a two-time energy measurement scheme [71]. However, in a full thermalization process, the measurement of energy at the end of the process is uncorrelated with the measurement at the start. Then, two QSTs are enough to provide a direct evaluation of the heat probability distribution in the present implementation [63]. One of them is done at the end of the energy gap expansion stroke (where the state is typically out-of-equilibrium), while the other is done at the start of the energy gap compression stroke (and thus should result in the hot thermal state). So the mean heat from the hot source can be expressed as $\langle Q_{\text{hot}} \rangle = \int dQ \mathcal{P}(Q) Q$.

With the aforementioned data, we have fully characterized the quantum heat engine. Its performance can be rated according to the average work extracted per cycle, efficiency, efficiency lag, and the average delivered power. These figures of merit are shown in Fig. 3(a)-3(d). The work extraction regime requires a lower bound on the

driving time length, as can be seen in Fig. 3(a) and also was anticipated by condition (3). If the engine is operated at a too-fast driving time length τ (smaller than $\approx 200 \mu\text{s}$ in this case), the entropy production is so large that it is not possible to extract work. This entropy production decreases with a slower operation rate, although not monotonically. The latter fact is a consequence of the specific form of the Hamiltonian time modulation employed in our implementation and does not generalize to other drivings.

Figure 3(b) illustrates that slower operation leads to better efficiency. Nonetheless, the quantum engine irreversibility can also be characterized by the efficiency lag (5) measured by QST at different strokes. We observe a complete agreement between the lag displayed in Fig. 3(c) and the efficiency measured as the mean work and heat ratio [Fig. 3(b)]. For the implemented quantum cycle, the main source of irreversibility is the divergence (accounted by the relative entropy) of the state achieved after the Hamiltonian driving protocols (expansion and compression) and the reference (hot and cold) thermal states.

We are often interested in power, and a too-slow engine operation, as an adiabatic dynamics, cannot deliver a fairly good amount of power. Extracted power is maximized when the energy gap expansion (compression) protocol takes about $310 \mu\text{s}$ as can be noted in Fig. 3(d). Quicker protocols are worse due to considerable entropy production associated with energy level transitions during the dynamics [Fig. 3(c)], while slower driven protocols are also worse since they take more time to deliver a similar amount of work [Fig. 3(a)]. The effective full thermalization with the hot source (^1H nucleus) employed in our experiment [central part of the pulse sequence in Fig. 1(b)] lasts for about 7 ms and it takes the same time length in all operation modes of the spin engine. In this fashion, we have opted to describe all results in terms of the expansion and compression Hamiltonian driving time length τ , which is the finite-time feature in the present spin engine implementation.

We performed an experimental proof-of-concept of a quantum heat engine based on a nuclear spin where the typical energy gaps, about 8.27 peV, are of the order of heat source energy, $k_B(T_2 - T_1)$ (≈ 15 peV). The extracted work per cycle may be on the same order of magnitude (few peV) depending on the driving protocol. At maximum power ($\tau \approx 310 \mu\text{s}$), the engine efficiency, $\eta = 42 \pm 6\%$, is very close to the Otto limit, $\eta_{\text{Otto}} = 44\%$, for the compression factor employed in the present implementation. The power delivered by the quantum engine, in the finite-time operation mode, is ultimately limited by quantum fluctuations (transitions among the instantaneous energy eigenstates), which are also related to entropy production [61, 65] leading to a “quantum friction” [29, 30]. Assessing the statistics of energy fluctuations in the implemented engine, we fully characterize its irreversibility and efficiency lag. The investigation of this data can also allow the quantum engine optimization by choosing optimal driving protocols.

The methods employed here to assess energy fluctuations and to characterize irreversibility in the quantum engine are versatile and can be applied to other experimental settings. The developed spin engine architecture is a comprehensive platform for future investigations of thermodynamical cycles at micro-scale, which would involve, for instance, non-equilibrium, non-classical, and correlated heat sources, allowing the detailed study of a plethora of effects in quantum thermodynamics [23, 24].

Acknowledgments. We thank E. Lutz, M. Paternostro, L. C. Céleri, C. I. Henao, P. A. Camati, K. Micadei, and F. L. Semião for valuable discussions. We acknowledge financial support from UFABC, CNPq, CAPES, FAPERJ, and FAPESP. J.P.S.P. thanks support from Innovation, Science and Economic Development Canada, the Government of Ontario, and CIFAR. T.B.B. acknowledges support from National Research Foundation (Singapore), Ministry of Education (Singapore), and United States Air Force Office of Scientific Research (FA2386-15-1-4082). R.M.S. gratefully acknowledges financial support from the Royal Society through the Newton Advanced Fellowship scheme (Grant no. NA140436) and the technical support from the Multiuser Experimental Facilities of UFABC. This research was performed as part of the Brazilian National Institute of Science and Technology for Quantum Information (INCT-IQ).

* These authors contributed equally to this work.

† [Electronic Address: serra@ufabc.edu.br](mailto:serra@ufabc.edu.br)

- [1] H. E. D. Scovil and E. O. Schulz-DuBois, Three-Level Masers as Heat Engines, *Phys. Rev. Lett.* **2**, 262 (1959).
- [2] R. Alicki, The quantum open system as a model of the heat engine, *J. Phys. A: Math. Gen.* **12**, L103-L107 (1979).
- [3] E. Geva and R. Kosloff, A quantum-mechanical heat engine operating in finite time. A model consisting of spin-1/2 systems as the working fluid, *J. Chem. Phys.* **96**, 3054-3067 (1992).
- [4] T. D. Kieu, The Second Law, Maxwell’s Demon, and Work Derivable from Quantum Heat Engines, *Phys. Rev. Lett.* **93**, 140403 (2004).
- [5] H. T. Quan, Y. xi Liu, C. P. Sun, and F. Nori, Quantum thermodynamic cycles and quantum heat engines, *Phys. Rev. E* **76**, 031105 (2007).
- [6] P. Hänggi and F. Marchesoni, Artificial Brownian motors: Controlling transport on the nanoscale, *Rev. Mod. Phys.* **81**, 387-442 (2009).
- [7] N. Linden, S. Popescu, and P. Skrzypczyk, How Small Can Thermal Machines Be? The Smallest Possible Refrigerator, *Phys. Rev. Lett.* **105**, 130401 (2010).
- [8] L. A. Correa, J. P. Palao, D. Alonso, and G. Adesso, Quantum-enhanced absorption refrigerators, *Sci. Rep.* **4**, 3949 (2014).
- [9] J. P. Palao, L. A. Correa, G. Adesso, and D. Alonso, Efficiency of inefficient endoreversible thermal machines, *Braz. J. Phys.* **46**, 282 (2015).
- [10] R. Uzdin and R. Kosloff, The multilevel four-stroke swap engine and its environment, *New J. Phys.* **16**, 095003 (2014).
- [11] R. Uzdin, A. Levy, and R. Kosloff, Equivalence of Quantum Heat Machines, and Quantum-Thermodynamic Signatures, *Phys. Rev. X* **5**, 031044 (2015).
- [12] F. C. Binder, S. Vinjanampathy, K. Modi, and J. Goold, Quantacell: powerful charging of quantum batteries, *New J. Phys.* **17**, 075015 (2015).
- [13] D. Gelbwaser-Klimovsky, R. Alicki, and G. Kurizki, Minimal universal quantum heat machine, *Phys. Rev. E* **87**, 012140 (2013).
- [14] M. O. Scully, M. S. Zubairy, G. S. Agarwal, and H. Walther, Extracting Work from a Single Heat Bath via Vanishing Quantum Coherence, *Science* **299**, 862 (2003).
- [15] N. Brunner, N. Linden, S. Popescu, and P. Skrzypczyk, Virtual qubits, virtual temperatures, and the foundations of thermodynamics, *Phys. Rev. E* **85**, 051117 (2012).
- [16] R. Gallego, A. Riera, and J. Eisert, Thermal machines beyond the weak coupling regime, *New J. Phys.* **16**, 125009 (2014).
- [17] R. Kosloff and A. Levy, Quantum Heat Engines and Refrigerators: Continuous Devices, *Annu. Rev. Phys. Chem.* **65**, 365-393 (2014).
- [18] A. Mari, A. Farace, and V. Giovannetti, Quantum optomechanical piston engines powered by heat, *J. Phys. B: At. Mol. Opt. Phys.* **48**, 175501 (2015).
- [19] N. Killoran, S. F. Huelga, and M. B. Plenio, Enhancing light-harvesting power with coherent vibrational interactions: A quantum heat engine picture, *J. Chem. Phys.* **143**, 155102 (2015).
- [20] A. Alecce, F. Galve, N. Lo Gullo, L. Dell’Anna, F. Plastina, and R. Zambrini, Quantum Otto cycle with inner friction: finite-time and disorder effects, *New J. Phys.* **17**, 075007 (2015).
- [21] P. P. Hofer, M. Perarnau-Llobet, J. B. Brask, R. Silva, M. Huber, and N. Brunner, Autonomous Quantum Refrigerator in a Circuit-QED Architecture Based on a Josephson Junction, *Phys. Rev. B* **94**, 235420 (2016).
- [22] M. Campisi and R. Fazio, The power of a critical heat engine, *Nat. Commun.* **7**, 11895 (2016).
- [23] J. Goold, M. Huber, A. Riera, L. del Rio, and P. Skrzypczyk, The role of quantum information in thermo-

- dynamics – a topical review, *J. Phys. A: Math. Theor.* **49**, 143001 (2016).
- [24] S. Vinjanampathy and J. Anders, Quantum thermodynamics, *Contemp. Phys.* **57**, 545 (2016).
- [25] C. Elouard, D. Herrera-Martí, B. Huard, and A. Auffèves, Extracting work from quantum measurement in Maxwell demon engines, *Phys. Rev. Lett.* **118**, 260603 (2017).
- [26] A. Dechant, N. Kiesel, E. Lutz, All-Optical Nanomechanical Heat Engine, *Phys. Rev. Lett.* **114**, 183602 (2015).
- [27] G. Watanabe, B. P. Venkatesh, P. Talkner, and A. del Campo, Quantum Performance of Thermal Machines over Many Cycles, *Phys. Rev. Lett.* **118**, 050601 (2017).
- [28] B. Reid, S. Pigeon, M. Antezza, and G. De Chiara, A self-contained quantum harmonic engine, *EPL (Europhysics Letters)* **120**, 6 (2018).
- [29] T. Feldmann and R. Kosloff, Quantum four-stroke heat engine: Thermodynamic observables in a model with intrinsic friction, *Phys. Rev. E* **68**, 016101 (2003).
- [30] F. Plastina, A. Alecce, T. J. G. Apollaro, G. Falcone, G. Francica, F. Galve, N. Lo Gullo, and R. Zambrini, Irreversible Work and Inner Friction in Quantum Thermodynamic Processes, *Phys. Rev. Lett.* **113**, 260601 (2014).
- [31] N. Shiraishi and H. Tajima, Efficiency versus speed in quantum heat engines: Rigorous constraint from Lieb-Robinson bound, *Phys. Rev. E* **96**, 022138 (2017).
- [32] G. Benenti, G. Casati, K. Saito, and R. S. Whitney, Fundamental aspects of steady-state conversion of heat to work at the nanoscale, *Phys. Rep.* **694**, 1 (2017).
- [33] M. Esposito, U. Harbola, and S. Mukamel, non-equilibrium fluctuations, fluctuation theorems, and counting statistics in quantum systems, *Rev. Mod. Phys.* **81**, 1665 (2009).
- [34] M. Campisi, P. Hänggi, and P. Talkner, Colloquium: Quantum fluctuation relations: Foundations and applications, *Rev. Mod. Phys.* **83**, 771 (2011).
- [35] P. Hänggi and P. Talkner, The other QFT, *Nat. Phys.* **11**, 108 (2015).
- [36] M. Campisi, Fluctuation relation for quantum heat engines and refrigerators, *J. Phys. A: Math. Theor.* **47**, 245001 (2014).
- [37] M. Campisi, J. Pekola, and R. Fazio, non-equilibrium fluctuations in quantum heat engines: theory, example, and possible solid state experiments, *New J. Phys.* **17**, 035012 (2015).
- [38] O. Abah, J. Roßnagel, G. Jacob, S. Deffner, F. Schmidt-Kaler, K. Singer, and E. Lutz, Single-Ion Heat Engine at Maximum Power, *Phys. Rev. Lett.* **109**, 203006 (2012).
- [39] J. Roßnagel, O. Abah, F. Schmidt-Kaler, K. Singer, and E. Lutz, Nanoscale Heat Engine Beyond the Carnot Limit, *Phys. Rev. Lett.* **112**, 030602 (2014).
- [40] D. M. Kennes, D. Schuricht, and V. Meden, Efficiency and power of a thermoelectric quantum dot device, *Europhys. Lett.* **102**, 57003 (2013).
- [41] R. Sánchez, B. Sothmann, A. N. Jordan, and M. Büttiker, Correlations of heat and charge currents in quantum-dot thermoelectric engines, *New J. Phys.* **15**, 125001 (2013).
- [42] B. Sothmann and R. Sánchez, and A. N. Jordan, Thermoelectric energy harvesting with quantum dots, *Nanotechnology* **26**, 032001 (2014).
- [43] T. L. van den Berg, F. Brange, and P. Samuelsson, Energy and temperature fluctuations in the single electron box, *New J. Phys.* **17**, 075012 (2015).
- [44] K. Zhang, F. Bariani, and P. Meystre, Quantum Optomechanical Heat Engine, *Phys. Rev. Lett.* **112**, 150602 (2014).
- [45] C. Bergenfeldt, P. Samuelsson, B. Sothmann, C. Flindt, and M. Büttiker, Hybrid Microwave-Cavity Heat Engine, *Phys. Rev. Lett.* **112**, 076803 (2014).
- [46] C. Elouard, M. Richard, and A. Auffèves, Reversible work extraction in a hybrid opto-mechanical system, *New J. Phys.* **17**, 055018 (2015).
- [47] M. Brunelli, A. Xuereb, A. Ferraro, G. De Chiara, N. Kiesel, and M. Paternostro, Out-of-equilibrium thermodynamics of quantum optomechanical systems, *New J. Phys.* **17**, 035016 (2015).
- [48] T. Hugel, N. B. Holland, A. Cattani, L. Moroder, M. Seitz, and H. E. Gaub, Single-Molecule Optomechanical Cycle, *Science* **296**, 1103 (2002).
- [49] P. G. Steeneken, K. Le Phan, M. J. Goossens, G. E. J. Koops, G. J. A. M. Brom, C. van der Avoort, and J. T. M. van Beek, Piezoresistive heat engine and refrigerator, *Nat. Phys.* **7**, 354 (2011).
- [50] V. Blickle and C. Bechinger, Realization of a micrometersized stochastic heat engine, *Nat. Phys.* **8**, 143 (2012).
- [51] J.-P. Brantut, C. Grenier, J. Meineke, D. Stadler, S. Krinner, C. Kollath, T. Esslinger, and A. Georges, A Thermoelectric Heat Engine with Ultracold Atoms, *Science* **342**, 713 (2013).
- [52] H. Thierschmann, R. Sánchez, B. Sothmann, F. Arnold, C. Heyn, W. Hansen, H. Buhmann, and L. W. Molenkamp, Three-terminal energy harvester with coupled quantum dots, *Nat. Nanotechnol.* **10**, 854 (2015).
- [53] F. Schmidt, A. Magazzù, A. Callegari, L. Biancofiore, F. Cichos, and G. Volpe, Microscopic Engine Powered by Critical Demixing, *Phys. Rev. Lett.* **120**, 068004 (2018).
- [54] J. Roßnagel, S. T. Dawkins, K. N. Tolazzi, O. Abah, E. Lutz, F. Schmidt-Kaler, and K. Singer, A single-atom heat engine. *Science* **352**, 325 (2016).
- [55] V. Holubec and A. Ryabov, Work and power fluctuations in a critical heat engine, *Phys. Rev. E* **96**, 030102, (2017).
- [56] I. S. Oliveira, T. J. Bonagamba, R. S. Sarthour, J. C. C. Freitas, and E. R. deAzevedo, *NMR Quantum Information Processing* (Elsevier, Amsterdam, 2007).
- [57] R. Dorner, S.R. Clark, L. Heaney, R. Fazio, J. Goold, and V. Vedral, Extracting quantum work statistics and fluctuation theorems by single-qubit interferometry, *Phys. Rev. Lett.* **110**, 230601 (2013).
- [58] L. Mazzola, G. De Chiara, and M. Paternostro, Measuring the characteristic function of the work distribution, *Phys. Rev. Lett.* **110**, 230602 (2013).
- [59] T. B. Batalhão, A. M. Souza, L. Mazzola, R. Auccaise, R. S. Sarthour, I. S. Oliveira, J. Goold, G. De Chiara, M. Paternostro, and R. M. Serra, Experimental Reconstruction of Work Distribution and Study of Fluctuation Relations in a Closed Quantum System, *Phys. Rev. Lett.* **113**, 140601 (2014).
- [60] J. Goold, U. Poschinger, and K. Modi, Measuring the heat exchange of a quantum process, *Phys. Rev. E* **90**, 020101 (2014).
- [61] T. B. Batalhão, A.M. Souza, R.S. Sarthour, I.S. Oliveira, M. Paternostro, E. Lutz, R.M. Serra, Irreversibility and the Arrow of Time in a Quenched Quantum System. *Phys. Rev. Lett.* **115**, 190601 (2015).
- [62] K. Micadei, J. P. S. Peterson, A. M. Souza, R. S. Sarthour, I. S. Oliveira, G. T. Landi, T. B. Batalhão, R. M. Serra, and E. Lutz, Reversing the direction of heat

- flow using quantum correlations, Nat. Comm. **10**, 2456 (2019).
- [63] See Supplemental Material at [URL will be inserted by publisher] for more details.
- [64] P. A. Camati and R. M. Serra, Verifying detailed fluctuation relations for discrete feedback-controlled quantum dynamics, Phys. Rev. A **97**, 042127 (2018).
- [65] P. A. Camati, J. P. S. Peterson, T. B. Batalhão, K. Micaidei, A. M. Souza, R. S. Sarthour, I. S. Oliveira, and R. M. Serra, Experimental Rectification of Entropy Production by Maxwell’s Demon in a Quantum System, Phys. Rev. Lett. **117**, 240502 (2016).
- [66] K. Brandner and U. Seifert, Periodic thermodynamics of open quantum systems. Phys. Rev. E, **93**, 062134 (2016).
- [67] K. Brandner, M. Bauer, and U. Seifert, Universal Coherence Induced Power Losses of Quantum Heat Engines in Linear Response, Phys. Rev. Lett. **119**, 170602 (2017).
- [68] P. A. Camati, J. F. G. Santos, and R. M. Serra, Coherence effects in the performance of the quantum Otto heat engine, Phys. Rev. A **99**, 062103 (2019).
- [69] I. L. Chuang and M. A. Nielsen, Prescription for experimental determination of the dynamics of a quantum black box, J. Mod. Opt. **44**, 2455 (1997).
- [70] M. A. Nielsen and I. L. Chuang, *Quantum Computation and Quantum Information* (Cambridge University Press, 2011).
- [71] P. Talkner, E. Lutz, and P. Hänggi, Fluctuation theorems: Work is not an observable, Phys. Rev. E **75**, 050102(R) (2007).

SUPPLEMENTAL MATERIAL

We provide here supplementary details about the experimental protocol and data analysis.

Experimental setting and characterization of the initial state preparation

The liquid sample comprises 50 mg of 99% ^{13}C -labeled CHCl_3 (Chloroform) diluted in 0.7 ml of 99.9% deuterated Acetone- d_6 , in a flame sealed 5 mm NMR tube. The experiments were performed in a Varian 500 MHz Spectrometer equipped with a double-resonance probe-head. The sample is inserted at the center of a superconducting magnet (immersed in liquid He inside a thermally shielded vessel) within the radio frequency (rf) coil of the inner probe head. The superconducting magnet produces a high intensity static magnetic field in the longitudinal direction (which defines the z axis). Magnetization of the ^1H and ^{13}C nuclear spins (with Larmor frequencies about 500 MHz and 125 MHz, respectively) can be controlled by time-modulated rf-field pulses in the transverse (x and y) direction and longitudinal field gradient pulses.

Employing spatial average techniques, the ^1H and ^{13}C nuclei are initially prepared in a pseudo-state equivalent to a tensor product, $\rho_0^{eq,2} \otimes \rho_0^{eq,1}$, of thermal Gibbs states, at spin temperatures T_2 (hot) and T_1 (cold), see also the

description of the thermal state initialization method in Ref. [62]. The initial pseudo-thermal state is certified by quantum state tomography (QST) [56]. The effective spin temperature of the initial ^1H (^{13}C) Gibbs state is related to the ground, $p_0^{\text{H(C)}}$, and excited, $p_1^{\text{H(C)}}$, populations as $k_B T_{2(1)} = h\nu_{2(1)} \left(\ln \frac{p_0^{\text{H(C)}}}{p_1^{\text{H(C)}}} \right)^{-1}$. From the QST tomography data we verified the initial spin temperature as displayed in Tab. SI.

Table SI. Population and spin temperatures of the Hydrogen and Carbon nuclei initial states. The coherence (off-diagonal) elements of initial pseudo-thermal states are null within the measurement error.

^1H nucleus	p_0^{H}	p_1^{H}	$k_B T_2$ (peV)
option A	0.67 ± 0.01	0.33 ± 0.01	21.5 ± 0.4
option B	0.60 ± 0.01	0.42 ± 0.01	40.5 ± 3.7
^{13}C nucleus	p_0^{C}	p_1^{C}	$k_B T_1$ (peV)
	0.78 ± 0.01	0.22 ± 0.01	6.6 ± 0.1

Energy gap expansion and compression protocols

The energy gap expansion and compression driven protocols are implemented by a time-modulated rf field set at the Carbon Larmor frequency, in order to produce the dynamics described by the time-dependent Hamiltonians $\mathcal{H}_{exp}^{\text{C}}(t)$ and $\mathcal{H}_{comp}^{\text{C}}(t)$, as defined in the main text. The time lengths of the driving processes implemented (i.e. $\tau = 100, 200, 235, 260, 300, 320, 420, 500, 600,$ and $700 \mu\text{s}$) are much shorter than the typical decoherence time scale. Spin-lattice relaxation times for the Hydrogen and Carbon nuclear spins are $\mathcal{T}_1^{\text{H}} = 7.42$ s and $\mathcal{T}_1^{\text{C}} = 11.31$ s, respectively. Transverse relaxations were measured as $\mathcal{T}_2^{*\text{H}} = 1.11$ s and $\mathcal{T}_2^{*\text{C}} = 0.30$ s. Besides the decoherence phenomenon that has a small effect in the driving dynamics, experimental imperfections and non-idealities prevent the realization of a perfectly unitary evolutions associated with the driving Hamiltonians. In order to verify the actually implemented protocol, we employed quantum process tomography (QPT) [69, 70].

A general description of a quantum dynamics as a map $\mathcal{E}(\rho)$ acting on an initial density operator, can be done in terms of the Choi-Jamiolkowski matrix, Υ , through the relation

$$\mathcal{E}(\rho) = \sum_{k,j=0}^3 \Upsilon_{k,j} \Xi_k \rho \Xi_j^\dagger, \quad (\text{S1})$$

where $\Xi_0 = i\mathbf{1}$ and (Ξ_1, Ξ_2, Ξ_3) are the Pauli operators $(\sigma_x, \sigma_y, \sigma_z)$. When written in this operator basis, any unital process (the one that preserve the identity $\mathcal{E}(\mathbf{1}) = \mathbf{1}$) corresponds to a real process matrix Υ .

We have prepared the ^{13}C nuclear spin in a set of states of a mutually unbiased basis (MUB) [69, 70], subjected

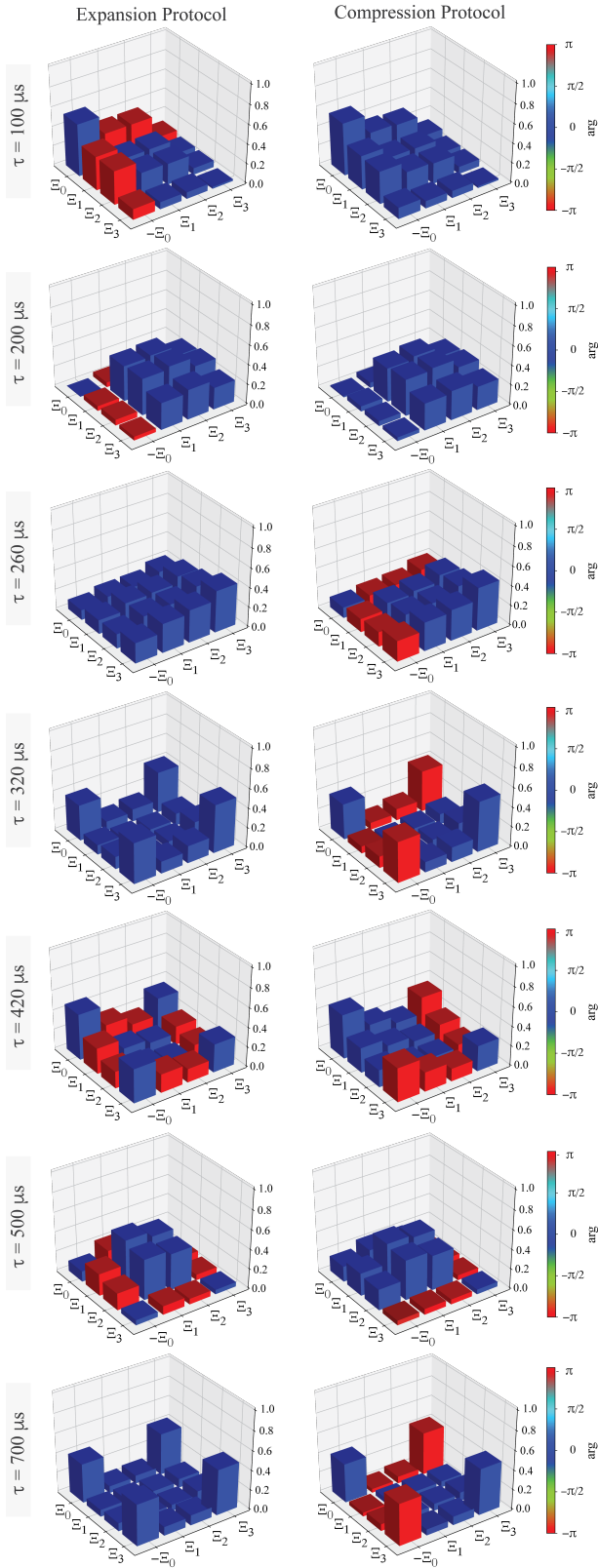


Figure S1. Quantum process tomography experimental data. Process matrix representation of the energy gap expansion and compression protocol. The height of each element is proportional to its absolute value and the color depends on its complex phase. Blue bars represent real positive values, while red bars represent real negative elements. The imaginary part of each element is approximately null within the experimental error.

each of them to the expansion (compression) protocol to be characterized, and finally reconstructed the output density matrix using QST. Numerical post processing of the acquired data enables the final estimate of the process matrix Υ elements. A summary of the results is shown in Fig. S1. The height of each element plotted in Fig. S1 is proportional to its absolute value, while the color depends on its complex phase. We see that every element is either blue (representing real positive elements) or red (representing real negative values), which is a visual indication that the process is unital. In a more quantitative analysis, typical values of the imaginary part are zero inside QST measurement precision. We have also checked that the expansion and compression processes, when applied in sequence, yields the identity process, and found about 95% fidelity between a state and the result of applying both processes to that state. It confirms that the compression protocol is, in a good approximation, the time reversal version of the expansion protocol.

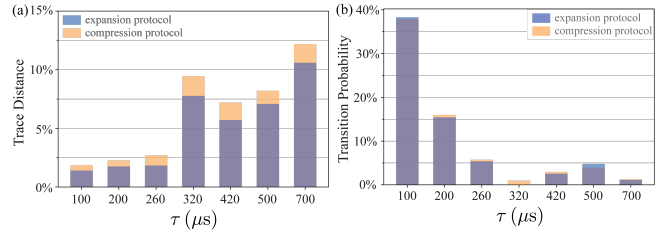


Figure S2. Characterization of the implemented driving protocols. (a) Deviation from a unitary evolution obtained from the QPT data quantifies by the process trace distance (δ). (b) Transition probability among the instantaneous eigenstates (ξ), obtained from the work probability distribution data, as a function of the Hamiltonian driving protocol time length (τ).

From the eigenvalues and “eigenoperators basis” of the Choi-Jamiolkowski matrix, we can check the closest unitary map to the experimentally implemented process. The process trace distance, $\delta = \frac{1}{2} \text{tr} |\Upsilon^{exp} - \Upsilon^{id}|$, between the map that describes the experimentally implemented driving protocol (Υ^{exp}) and the ideal unitary map (Υ^{id}) is plotted in Fig. S2(a). It is associated with the bias for distinguishing between the ideal and experimental processes. We observe that the implemented driving protocols are almost unitary for the fast-driving dynamics ($\delta < 3\%$), as the time length is increased the process trace distance also increases, but it still relatively small (less than 12% for $\tau = 700 \mu\text{s}$) validating our approximation of the driving processes as quasi-unitary. This small increasing in the process trace distance when we increase τ is mainly due to spatial non-homogeneity of time-modulated rf pulse and the transverse relaxation (which has more effect on long dynamics).

Heating protocol

From the local point of view of the Carbon nucleus the heating evolution, has the effect of a linear non-unitary map $\mathcal{E}(\rho_i) = \text{Tr}_i(\mathcal{U}_\tau \rho_A^0 \otimes \rho_B^0 \mathcal{U}_\tau^\dagger)$ on the working substance, which can be represented as

$$\mathcal{E}(\rho_i) = \sum_{j=1}^4 K_j \rho_i^0 K_j^\dagger \quad (\text{S2})$$

where $i = A, B$. The Kraus operators are given by

$$\begin{aligned} K_1 &= \sqrt{1-p} \begin{bmatrix} 1 & 0 \\ 0 & 0 \end{bmatrix}, & K_3 &= \sqrt{p} \begin{bmatrix} 0 & 0 \\ 0 & 1 \end{bmatrix}, \\ K_2 &= \sqrt{1-p} \begin{bmatrix} 0 & 1 \\ 0 & 0 \end{bmatrix}, & K_4 &= \sqrt{p} \begin{bmatrix} 0 & 0 \\ -1 & 0 \end{bmatrix}, \end{aligned}$$

with p being the population of the excited state in the Hydrogen nucleus.

This map is equivalent to the *generalized amplitude damping* which is the Kraus map for the thermalization (in this case full thermalization) of a single spin-1/2 system. Therefore, from the local point of view of the working substance, the interaction with the "hot spin system" in the experiment is indistinguishable from a thermalization map. This plays the role of an effective thermalization in our proof of concept experiment.

Control rotations perform no work in the engine protocol

Consider a single rotation (represented by the red and blue circles in the pulse sequence description) implemented by a hard square rf pulse on resonance with the nuclear spin A. The Hamiltonian of the system, in the rotation frame with the Larmor frequency of the nuclear spin A, can be effectively described as

$$\mathcal{H} = u(t)\mathcal{V}_A, \quad (\text{S3})$$

where $u(t) = \theta(t) - \theta(t - t')$ can very well modeled as the sum of two (unity) Heaviside functions ($\theta(x)$) such that $u(t)$ is 1 if $0 < t < t'$ and 0 if $t < 0$ or $t > 0$ and \mathcal{V}_A is the potential generated by the transverse rf field. The mean work performed in the process of turning on and off the rf pulse between the two spin systems can be unambiguously defined as

$$\langle W \rangle = \int_{-\infty}^{\infty} dt \left\langle \frac{\partial \mathcal{H}}{\partial t} \right\rangle_t \quad (\text{S4})$$

Since $\dot{u}(t) = \delta(t) - \delta(t - t')$ (where $\delta(x)$ is the Dirac delta function), it follows that

$$\langle W \rangle = \langle \mathcal{V}_A \rangle_0 - \langle \mathcal{V}_A \rangle_{t'} = 0. \quad (\text{S5})$$

Hence, no work is performed when the transient time for turning on and off the time-independent rf rotation pulse is sufficiently small to be modelled as (unity) Heaviside functions, which is precisely the case in our experiment.

Extracted work statistics

The extracted work from (work performed on) the ^{13}C nuclear spin during the Otto cycle is a stochastic variable with a probability distribution written in terms of a characteristic function as

$$P_{eng}(W) = \int du \chi_{eng}(u) e^{iuW}. \quad (\text{S6})$$

The work characteristic function of the spin engine performing the quantum Otto cycle (with full thermalization) can be written as

$$\begin{aligned} \chi_{eng}(u) &= \chi_{comp}(u) \chi_{exp}(u) \\ &= \sum_{n,m,k,j=0}^1 p_n^0 p_m^\tau q_k^0 q_j^\tau e^{iu(\epsilon_m^\tau - \epsilon_n^0 + \epsilon_j^0 - \epsilon_k^\tau)}, \quad (\text{S7}) \end{aligned}$$

where p_n^0 is the occupation probability of the n -th energy level in the initial cold thermal state ($\rho_0^{\text{eq},1}$), $p_m^\tau = |\langle m^{(\tau)} | \mathcal{U}_\tau | n^{(0)} \rangle|^2$ is the transition probability between the instantaneous eigenstates $|n^{(0)}\rangle$ ($|m^{(\tau)}\rangle$) of the driving Hamiltonian $\mathcal{H}_{exp}^C(0)$ ($\mathcal{H}_{exp}^C(\tau)$), q_k^0 is the occupation probability of the k -th energy level in the equilibrium state ($\rho_0^{\text{eq},2}$) after the thermalization with the hot source, $q_m^\tau = |\langle j^{(\tau)} | \mathcal{V}_\tau | k^{(0)} \rangle|^2$ is transition probability between the instantaneous eigenstates $|k^{(0)}\rangle$ ($|j^{(\tau)}\rangle$) of the driving Hamiltonian $\mathcal{H}_{comp}^C(0)$ ($\mathcal{H}_{comp}^C(\tau)$), ϵ_m^τ and ϵ_n^0 are eigenvalues of the Hamiltonians \mathcal{H}_2^C and \mathcal{H}_1^C (defined in the main text), respectively.

The work characteristic function of the spin engine can be rewritten as

$$\begin{aligned} \chi_{eng}(u) &= \text{tr} \left[\mathcal{U}_\tau e^{-iu\mathcal{H}_{exp,0}^C} \rho_0^{\text{eq},1} \left(e^{-iu\mathcal{H}_{exp,\tau}^C} \mathcal{U}_\tau \right)^\dagger \right] \\ &\quad \times \text{tr} \left[\mathcal{V}_\tau e^{-iu\mathcal{H}_{comp,0}^C} \rho_0^{\text{eq},2} \left(e^{-iu\mathcal{H}_{comp,\tau}^C} \mathcal{V}_\tau \right)^\dagger \right]. \quad (\text{S8}) \end{aligned}$$

Each trace (associated with the expansion and compression drivings) in the product of rhs of Eq. (S8) was measured by an adaptation of the interferometric protocol described in Refs. [59, 61].

As a consequence of the finite-time dynamics produced by the driving protocol and the thermalization process, transitions between the instantaneous energy eigenstates

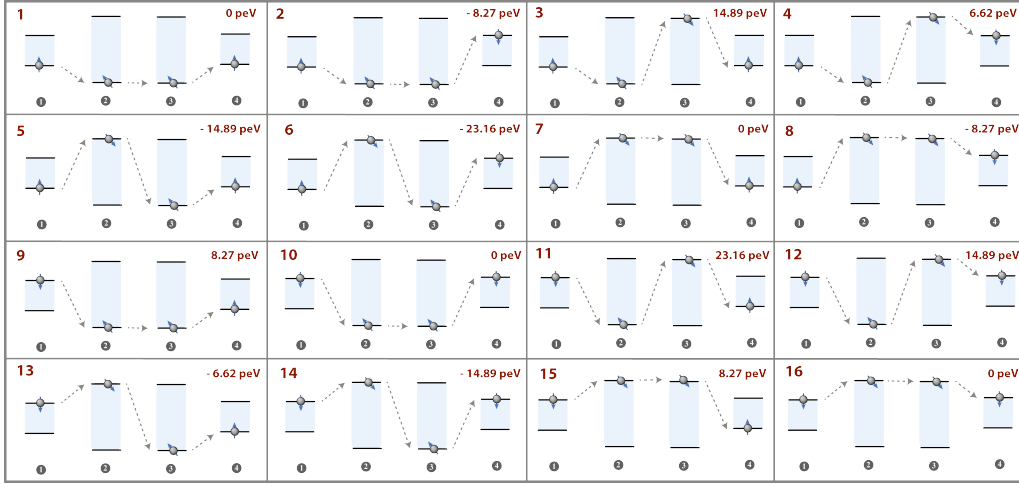


Figure S3. Transitions between the instantaneous energy eigenstates of the spin-1/2 working medium performing the quantum Otto cycle. There are sixteen possible energy-transition combinations in the spin engine. Variation in the internal energy of each transition history is displayed on the top right side of each inner box. The implemented four-stroke cycle is illustrated as follows: (1) ^{13}C nucleus starts in the cold thermal state; (2) it is driven by a time-modulated rf field that expand the energy gap resulting in a out-of-equilibrium state; (3) the working medium thermalizes with the hot source; (4) it is driven by the time reversal protocol that compress the energy gap.

of the working medium may occur. Figure S3 illustrates the sixteen possible energy-transition combinations of the spin engine performing the Otto cycle. One or more histories of Fig. S3 are associated with each peak in the extracted work probability distribution plotted in Fig. 2 of the main text and in Fig. S4. For the sake of completeness, we plot in Fig. S4 the work probability distribution for driving time lengths not displayed in the main text. From the experimental statistics of work, we determined the transition probability among the instantaneous eigenstates (ξ) as shown in Fig. S2(b). As expected for a fast Hamiltonian driving, we have a big transition probability (about 38% for $\tau = 100 \mu\text{s}$). As the driving time length increases, the transition probability decreases readily (reaching about 2% for $\tau = 700 \mu\text{s}$), since we are getting close to an adiabatic evolution.

Heat flow from the hot source

The heat exchanged between the working medium (^{13}C nuclear spin) and the hot source (^1H nuclear spin) in the heating stroke is also a stochastic variable with a heat characteristic function giving by

$$\chi_{Q_{hot}}(u) = \sum_{m,k=0}^1 \left(\sum_{n=0}^1 p_n^0 p_{m|n}^\tau \right) q_k^0 e^{iu(\epsilon_m^\tau - \epsilon_k^\tau)}. \quad (\text{S9})$$

We note that the expression (S9) does not depends explicitly on the energy level transitions ($p_{m|n}^\tau$) due to the expansion driving protocol. It only depends on the occupation probability of the energy levels of the Hamil-

tonian \mathcal{H}_2^C just after the expansion driving protocol, $s_m = \sum_{n=0}^1 p_n^0 p_{m|n}^\tau$, that can be obtained through a QST performed before the heating stroke. The occupation probability of the k -th energy level after the thermalization with the hot source, q_k^0 , can also be obtained by QST. The marginal probability distribution for the heat from the hot source can be written as

$$\begin{aligned} \mathcal{P}(Q) &= \int du \chi_{Q_{hot}}(u) e^{-iuQ}, \\ &= \sum_{m,k=0}^1 \left(\sum_{n=0}^1 p_n^0 p_{m|n}^\tau \right) q_k^0 \delta(\epsilon_k^\tau - \epsilon_m^\tau - Q). \end{aligned} \quad (\text{S10})$$

The mean value of the absorbed heat from the hot source, $\langle Q_{hot} \rangle = \text{tr} \left[\mathcal{H}_{\text{exp},\tau}^C \left(\rho_0^{\text{eq},2} - \mathcal{U}_\tau \rho_0^{\text{eq},1} \mathcal{U}_\tau^\dagger \right) \right]$, can also be acquired from the direct observation of the variation of the ^{13}C nucleus magnetization before and after the heating process. Moreover, alternatively as another verification for the heat flow measurement, data from QST and QPT can be combined to reconstruct the working medium state at the beginning of each stroke in the Otto cycle. The data obtained from different strategies to determine the heat probability distribution is in good agreement.

Statistics of heat flow is gathered from the reconstructed density matrix and it is displayed in Fig. S5(a) for different Hamiltonian driving time lengths τ . The amount of heat exchanged with the hot source depends on the final state of the ^{13}C nucleus reached after the expansion driving protocol. In a fast energy expansion driving ($\tau = 100 \mu\text{s}$), the final state corresponds to a non-equilibrium state with not null coherences (non-diagonal

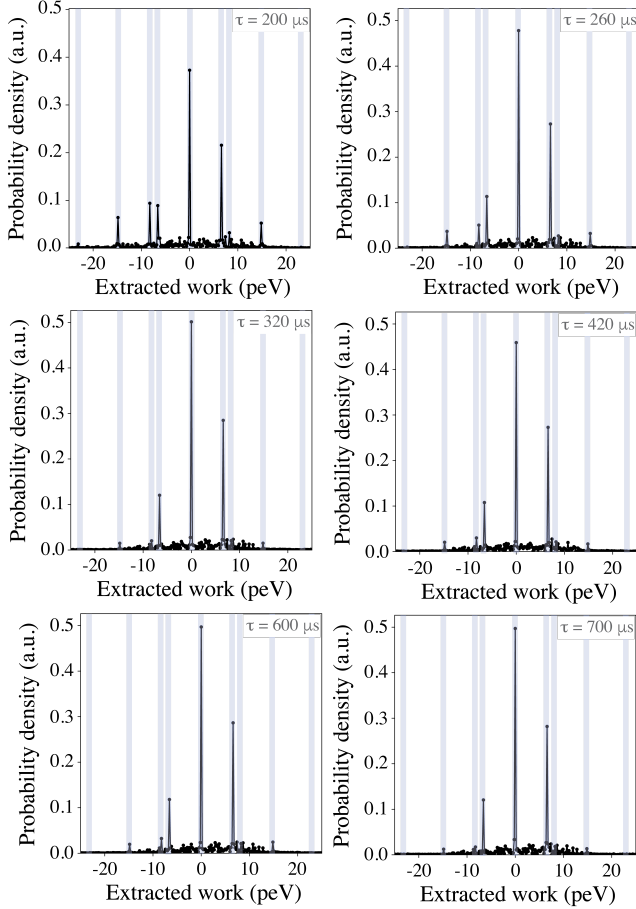


Figure S4. Extracted work probability distribution of the quantum engine with driving time lengths: $\tau = 200, 260, 320, 420, 600,$ and $700 \mu\text{s}$. Cold and hot source temperatures are set at $k_B T_1 = (6.6 \pm 0.1) \text{ peV}$ and $k_B T_2^B = (40.5 \pm 3.7) \text{ peV}$, respectively. The experimental data (points) is well fitted by a sum of nine Lorentzian peaks (the full line) centered approximately at $0, \pm 6.62, \pm 8.27, \pm 14.89,$ and $\pm 23.16 \text{ peV}$ (dashed columns), in agreement with the theoretical expectation (see Fig. S3). The error bars are smaller than the symbols size and are not shown.

elements) in the Hamiltonian basis turning the heat absorption less effective. On the other hand, in a slow energy expansion driving ($\tau = 700 \mu\text{s}$), the final state also corresponds to a non-equilibrium state, but the coherences elements in the Hamiltonian basis are much smaller (almost null). In fact, in the later case the state after energy expansion driving is very close to the state obtained in an adiabatic dynamics. The mean value of the absorbed heat ($\langle Q_{hot} \rangle$) as a function of the Hamiltonian driving protocol time length (τ) is shown in Fig. S5(b). The results obtained for the mean value of the absorbed heat ($\langle Q_{hot} \rangle$) are in complete agreement with the one obtained from the direct observation of the ^{13}C nucleus magnetization before and after the heating stroke.

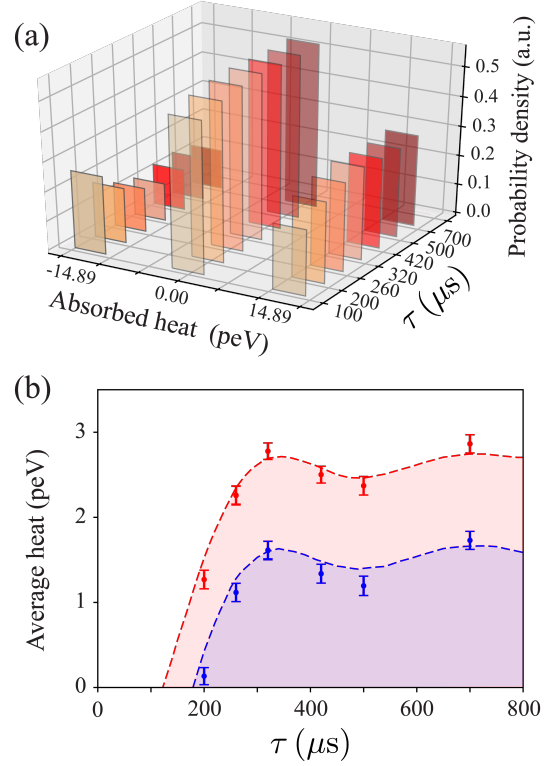


Figure S5. Absorbed heat from the hot source by the spin quantum engine. (a) Heat probability distribution, $\mathcal{P}(Q)$, with different Hamiltonian driving time lengths τ . Cold and hot source temperatures are set at $k_B T_1 = (6.6 \pm 0.1) \text{ peV}$ and $k_B T_2^B = (40.5 \pm 3.7) \text{ peV}$, respectively. The error bars are smaller than the size of the symbols and are not shown. (b) Average heat from the hot source, $\langle Q_{hot} \rangle$, as a function of τ . Points represent experimental data. The dashed lines are based on theoretical predictions and numerical simulations. In all experiments, the spin temperature of the cold source is set at $k_B T_1 = (6.6 \pm 0.1) \text{ peV}$. Data in blue and red correspond to implementations with the hot source spin temperatures set at $k_B T_2^A = (21.5 \pm 0.4) \text{ peV}$ and $k_B T_2^B = (40.5 \pm 3.7) \text{ peV}$, respectively.

Efficiency Lag (Eq. (5) of the main text)

In this section we will outline a demonstration of the expression for the Efficiency Lag introduced in Eq. (5) of the main text. Let us start with the sum of the entropy production in the expansion and compression driving protocols of the quantum Otto cycle, which can be expressed as the sum of two relative entropies that reads

$$\begin{aligned} \Sigma_{drive} &= \mathcal{S}(\rho_\tau^1 \| \rho_0^{eq,2}) + \mathcal{S}(\rho_\tau^2 \| \rho_0^{eq,1}) \\ &= \text{tr}(\rho_\tau^1 \ln \rho_\tau^1) - \text{tr}(\rho_\tau^1 \ln \rho_0^{eq,2}) \\ &\quad + \text{tr}(\rho_\tau^2 \ln \rho_\tau^2) - \text{tr}(\rho_\tau^2 \ln \rho_0^{eq,1}), \end{aligned} \quad (\text{S11})$$

where $\rho_\tau^1 = \mathcal{U}_\tau \rho_0^{eq,1} \mathcal{U}_\tau^\dagger$ is the final non-equilibrium state after the expansion protocol and $\rho_\tau^2 = \mathcal{V}_\tau \rho_0^{eq,2} \mathcal{V}_\tau^\dagger$ is the

final non-equilibrium state after the compression protocol. The von Neumann entropy is invariant under the unitary driving protocol, so it implies that $\text{tr}(\rho_\tau^\alpha \ln \rho_\tau^\alpha) = \text{tr}(\rho_0^\alpha \ln \rho_0^\alpha)$. Using this fact and recalling the form of the initial pseudo-thermal state, $\rho_0^{\text{eq},\alpha} = e^{-\beta_\alpha \mathcal{H}_\alpha^C} / Z_\alpha$, where $\alpha = 1, 2$, we obtain

$$\begin{aligned} \Sigma_{drive} = & -\beta_1 \text{tr} \left[\left(\rho_0^{\text{eq},1} - \rho_\tau^2 \right) \mathcal{H}_1^C \right] \\ & - \beta_2 \text{tr} \left[\left(\rho_0^{\text{eq},2} - \rho_\tau^1 \right) \mathcal{H}_2^C \right]. \end{aligned} \quad (\text{S12})$$

The last equation can be simplified to $\Sigma_{drive} = -\beta_1 \langle Q_{cold} \rangle - \beta_2 \langle Q_{hot} \rangle$, where $\langle Q_{cold} \rangle = \text{tr} \left[\left(\rho_0^{\text{eq},1} - \rho_\tau^2 \right) \mathcal{H}_1^C \right]$ and $\langle Q_{hot} \rangle = \text{tr} \left[\left(\rho_0^{\text{eq},2} - \rho_\tau^1 \right) \mathcal{H}_2^C \right]$. Employing the First Law of thermodynamics, $\langle Q_{cold} \rangle + \langle Q_{hot} \rangle - \langle W_{eng} \rangle = 0$, we can eliminate the heat from the cold source and write $\Sigma_{drive} = -\beta_1 \langle W_{eng} \rangle + (\beta_1 - \beta_2) \langle Q_{hot} \rangle$, which lead us to the relation

$$\frac{\langle W_{eng} \rangle}{\langle Q_{hot} \rangle} = \left(1 - \frac{T_1}{T_2} \right) - \frac{\mathcal{S} \left(\rho_\tau^1 \parallel \rho_0^{\text{eq},2} \right) + \mathcal{S} \left(\rho_\tau^2 \parallel \rho_0^{\text{eq},1} \right)}{\beta_1 \langle Q_{hot} \rangle}. \quad (\text{S13})$$

The lhs of Eq. (S13) can be identified as the efficiency of the quantum heat engine (η). The first and the second terms of the rhs are the Carnot limit (η_{Carnot}) and the efficiency lag (\mathcal{L}), respectively. The above development

demonstrates the definition introduced in Eq. (5) of the main text for the quantum Otto cycle. The efficiency lag, \mathcal{L} , describes the quantum engine irreversibility in terms of its microscopic state dynamics.

Error analysis

The most relevant sources of error in the experiments are small non-homogeneities of the transverse rf field, non-idealities in its time modulation, and non-idealities in the longitudinal field gradient. To estimate the error propagation, we have employed a Monte Carlo method, to sample deviations of the QST and magnetization data with a Gaussian distribution having widths determined by the corresponding variances. The standard deviation of the distribution of values for the relevant quantities is estimated from this sampling. The variances of the tomographic data are obtained by preparing the same state one hundred times, taking the full state tomography and comparing it with the theoretical expectation. These variances include random and systematic errors in both state preparation and data acquisition by QST. The error in each element of the density matrix estimated from this analysis is about 1%. All control parameters in the experimental implementation, such as pulse intensity, phase, and its time length, are optimized in order to minimize errors.